Research article

Microstructure and properties of a shape memory alloy Ti–Ni–Al–V fabricated by double-wire arc additive manufacturing

Xiaoxin Zhao [a,d,*], Xinya Chen [b], Tao Ma [c,d], Peng Zhang [c,d], Jianguo Li [c,d], Xin Zhang [e]

[a] *Research Center of Energy Engineering Advanced Joining Technology, Beijing Institute of Petrochemical Technology, Beijing 102627, China*
[b] *School of Materials Science and Engineering, Tianjin University of Technology, Tianjin 300382, China*
[c] *Inner Mongolia First Machinery Group Co., Ltd, Baotou 014030, China*
[d] *State Key Laboratory of Smart Manufacturing for Special Vehicles and Transmission System, Baotou 014030, China*
[e] *School of Automobile Engineering, Changshu Institute of Technology, Suzhou 215506, China*

A B S T R A C T

In this study, a novel heterogeneous double-wire arc additive manufacturing method was used for the in-situ synthesis of a novel Ti–Ni–Al–V alloy wall. The results indicated that the synthesis wall was composed of the $NiTi_2$, B_2, and Ni_4Ti_3 phases from the bottom to the top. With an increase in deposition layers, the Ti2Ni content decreased. The hardness at the bottom was ~685.4 $HV_{0.2}$, while that of the middle and stable regions was 553 $HV_{0.2}$. The maximum compressive strength was 2100 MPa. The fracture morphology was brittle. After cyclic compression, the recoverable and unrecoverable strains were 4.79 % and 1.21 %, respectively, indicating excellent recovery characteristics.

1. Introduction

Double-wire arc additive manufacturing (D-WAAM) has extremely high deposition velocity and material utilization [1]. Recently, several studies have explored the use of D-WAAM to fabricate materials without wires with a corresponding composition or high wire cost. A Ni–Ti–Cr–Mo–Nb alloy synthesis wall was fabricated in situ by D-WAAM using TA1 and Inconel 625 wires as the feedstock [2]. D-WAAM has also been used to reduce the fabrication cost of NiTi alloys [3]. Furthermore, an innovative Ti–6Al–4V-8.5Ni was fabricated via D-WAAM using both TC4 and pure Ni welding wires [4], indicating that D-WAAM technology has an ability to fabricate the parts which traditional WAAM is difficult or costly to prepare.

NiTi alloys are used in biomedicine, automobile, and aerocraft applications because of outstanding damping property, hyper-elasticitys, shape-memory function and high specific strength [5]. Based on the Ti–Ni binary alloy, an addition of Al, V, Cr, or Fe significantly changes the phase-transition temperature and critical slip stress of the material and effectively improves the NiTi alloy properties [6]. To date, no Ti–Ni–Al–V alloy has been studied. In general, Ni–Ti shape memory alloys are fabricated by casting and powder metallurgy, due to its severe brittleness and poor machinability, which always has the low efficiency, high cost, and worse dimensional stability [7]. Therefore, in traditional manufacturing, NiTi components are always wires, plate or bar. This hinders the application of NiTi function material severely. At present, Ni–Ti function material are manufactured through AM, which is a trend. The

---

Ni–Ti function material is always used as shape memory alloy. And it is manufactured through selective laser melting with a power of 65 W, which shows recoverable strain of 3.91 % at first cycle and about 3.88 % after ten times cyclic compression [8]. The approximately equal atom Ti-50.2Ni shape memory alloy is manufactured by laser powder bed fusion(LPBF). The result shows that heat cycling of the wall assembly with an annealing temperature of 400 °C obviously improves the elastic strains [9]. Using cold metal transfer, wall-shaped NiTi alloy with excellent homogeneity of the microhardness (~290 HV), critical stress (~600 MPa), and recoverable strain (~3 %) are manufactured [7]. A NiTi part was fabricated by WAAM technology. After twenty-five cycles, the best recovery rate and irrecoverable strain were almost 95 % and 0.09 %, respectively [10]. Homogeneous NiTi thin-walled components were manufactured using WAAM with different heat input, which showed superp abrasive resistance, the frictional coefficient decreased gradually with an incremental height of as-built wall [11]. Generally speaking, NiTi parts fabricated by WAAM exhibit superelastic behavior. The application is very promising for complex shape workpiece. However, the commercial Ni–Ti alloy wire is relatively rare and extremely expensive. To fabricate NiTi alloy with high efficiently and low cost, D-WAAM is a good choice due to its economical efficiency. The expensive NiTi welding wire is not used, instead of Ti and Ni wires with low cost.

In this study, using Ti–6Al–4V and pure Ni wires as raw materials, a Ti–Ni–Al–V alloy wall was manufactured in situ by D-WAAM, and its microstructures and properties were examined.

2. Experimental

A Ti–Ni–Al–V alloy wall was manufactured on a Ti–6Al–4V substrate with a wire feeding rate 1500 mm/min (Ti–6Al–4V) and 1045 mm/min (ER-Ni). The wire diameter was 1.2 mm. The macrostructure morphology was shown in Fig. 1(a). Before microstructure mechanical properties analysis, non destructive testing (NDT) was performed using penetrant testing as shown in Fig. 1(b). The white area indicates that no pore and cracks were found. In this study, all tested specimens were intercepted in the white area. However, on both sides of the deposition wall, the red color is observed, indicating that a defect is formed. The defect is a groove formed between layers, due to the effect of arcing and quenching, which is a common phenomenon during WAAM process. In the engineering application and test characterization process, the grooves on both sides are cut out.

The chemical compositions of the raw materials and the experimental system were the same as those in Ref. [12]. The interlayer residence time was 120 s. The substrate was heated to 400 °C. The temperature variation was measured during the process of additive manufacturing from 1st to 16th layer by a K mode thermocouple, which was layed in the center of the base metal and offset by 10 mm away from the heat source. The heat history data were recorded and managed. All the samples were taken from 1st to 16th layer. Prior to microanalysis and mechanical performance analysis, NDT was performed and no pore and cracks were found. A sample was taken from the as-built wall for metallographic analysis. Then the specimen was etched for about half a minute using a standard Keller's reagent. At room temperature, the phase compositions were detected using X-ray diffraction (XRD, D/tex Ultra 250) with CuKα radiation ($\lambda = 1.5418$ Å), scanning speed of 5 deg/min, and scanning range of 30°–80°. The microstructure was observed using scanning electron microscopy (SEM, S-4800, Hitachi) equipped with an energy dispersive spectrometer (EDS) and transmission electron microscopy (TEM, Tecnai F30, FEI). The Vickers microhardness was measured along the height direction. The load was set to 200 g, and the load duration was 15 s. Single/cycle compression experiments were performed on 3 samples with a dimension of φ 4 mm × 8 mm at normal temperature with a compression tester. The compression rate was 0.5 mm/min.

3. Results and discussion

3.1. Microstructure analysis

As shown in Fig. 2, the temperature rises sharply up to a maximum value due to the effect of heating process and gradually decreased during the heat source removal process. The thermal history indicates that the temperature is between 500 °C and 1250 °C during depositing layer 1 to layer 4. Start at the fifth layer, the temperature is between 500 °C and 800 °C. XRD can determine the crystal structure of the sample. Every material possesses a specific crystal structure in which atoms or molecules are arranged in a fixed mode. The XRD spectrum shows a series of peaks that correspond to the crystal faces in the sample. By comparing the positions and intensities of these peaks, the crystal structure of the substance can be determined. After the two metals melt into an alloy, their lattice will change. According to the basic principle of crystal diffraction, their XRD diffraction pattern will also change accordingly.
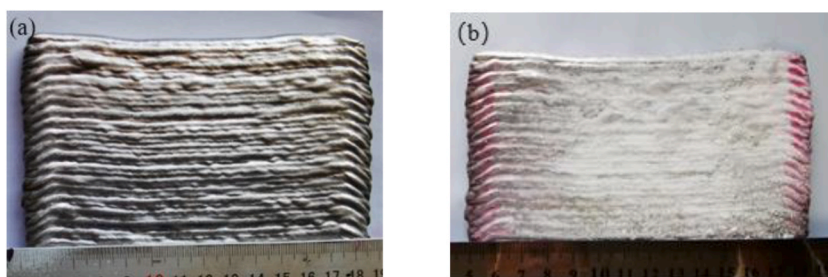

Fig. 1. Morphology of the (a) macrostructure, and (b) penetrant testing of the as-built wall.
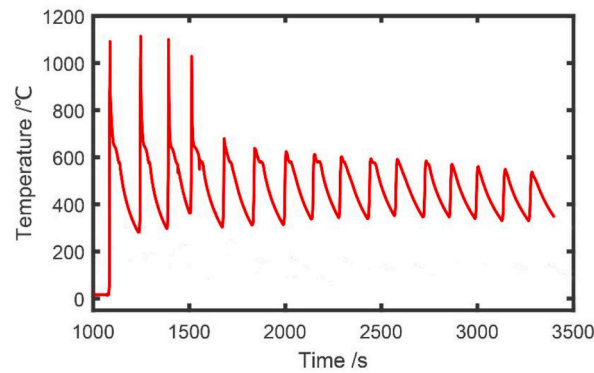
Fig. 2. Thermal history of the as-built wall.

Therefore, this change can be used to confirm whether the two are forming alloys. The XRD patterns of the as-built Ti–Ni–Al–V alloy wall at normal temperature are shown in Fig. 3(d). The abscissa is twice the X-ray incidence angle and the ordinate is the diffraction photon intensity. The peaks of pure Ni, α-Ti, and β-Ti are not found from bottom to top regions of the as-built wall, indicating that in-situ metallurgical reactions occurred in the two wires. From bottom to top area, the strongest peak was corresponding to B2 phase, indicating that the austenitic B2 NiTi phase was the matrix. Besides, $NiTi_2$ phase was obviously detected. As shown by the peak intensity of $NiTi_2$ phase, the phase content of Ni_4Ti_3 increases from bottom to top of the as-built wall. However, the intensity of Ni_4Ti_3 as a precipitate phase is low. The formation of Ni_4Ti_3 phase cannot be confirmed according to the XRD result, which needs to be verified by TEM. No additional phase is detected from bottom to top area. The Gibbs free energy of $NiTi_2$ and NiTi phases are −74.7 and −58.2 kJ/mol, respectively [13,14]. The Gibbs free energy of the $NiTi_2$ phase is lower than that of the NiTi phase. Thermodynamically, the formation of $NiTi_2$ phase is prior to that of the NiTi phase. Zou et al. [15] proposed that the primary $NiTi_2$ phase had a priority to develop into equiaxed dendritic crystals, while the other liquid phase developed into the NiTi phase. Therefore, during the process of cooling, the $NiTi_2$ phase had a formation priority. According to the Ti–Ni diagram, when the Ni:Ti ratio was 1:1, the B2 phase was formed in the liquid melting zone owing to the metallurgical reaction. The Ni_4Ti_3 phase diffusely precipitated from the supersaturated matrix by homogeneous nucleation. During additive manufacturing, the heat source remelts the previously deposited layer and heats the base material, which contributes to the production of the Ni_4Ti_3-precipitated phase.

TiNi and Ti_2Ni are shown at the bottom in Fig. 3(a). The substrate (Ti–6Al–4V) contained a large number of Ti atoms, which contributed to the formation of the Ti_2Ni phase at the bottom. According to the Ni–Ti diagram, Ti_2Ni was formed when the Ti content reached 66 at.%. In Fig. 3(b) and (c), several incomplete dendrites are observed in the middle, along with the precipitated phase (Ti_2Ni) in the middle and top in the form of dendrites. As the number of deposition layers increase, the content and size of Ti_2Ni decrease significantly and the NiTi content increased in the matrix. As shown in Table 1, Al- (9 at.%) and V-rich (3 at.%) phases are
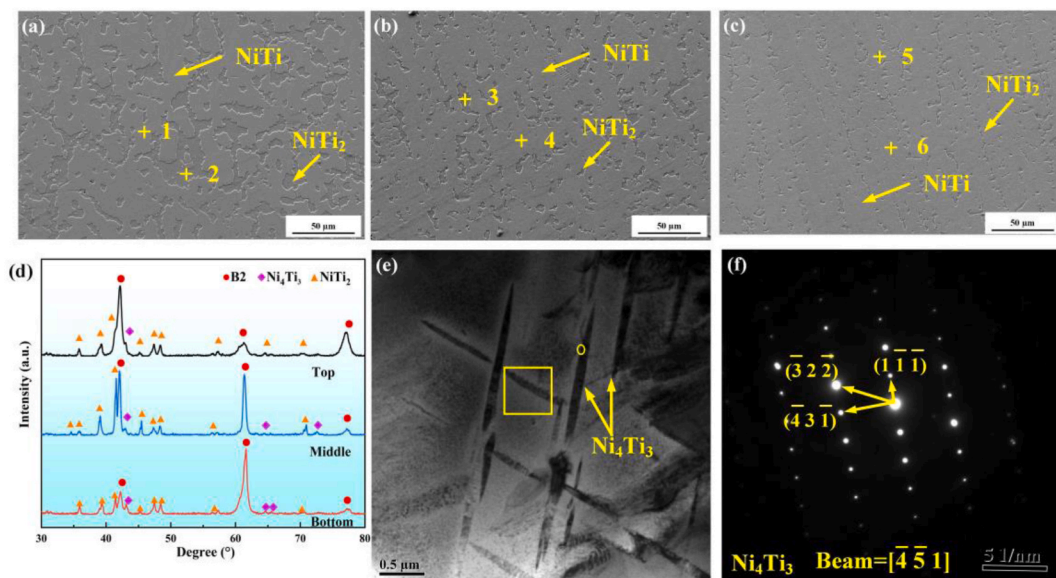

Fig. 3. Microstructure analysis of the Ti–Ni–Al–V alloy. SEM images of the (a) bottom, (b) middle, (c) top. (d) XRD of the as-built Ti–Ni–Al–V wall, (e) TEM image of the top, and (f) diffraction spots of the circle in Fig. 3(e).

present in Ti$_2$Ni, which originated from Ti–6Al–4V. Moreover, the Al content of NiTi was ~5.5.% in the form of a solid solution. The Ti$_4$Ni$_3$ phase is not detected by SEM in Fig. 3(e) and (f). However, a nanoprecipitated phase is observed at the top, which was confirmed as the Ti$_4$Ni$_3$ phase by TEM. The Ni$_4$Ti$_3$ phase typically maintains an excellent coherent relationship with the B2 matrix, and its coherent strain-field contrast changes with the increased size of the Ni$_4$Ti$_3$ phase. With the aggregation and grain coarsening of the Ni$_4$Ti$_3$ phase, the coherent relationship with the matrix was gradually lost, and dislocations occurred in the surrounding matrix.

3.2. Property analysis

As shown in Fig. 4(a), the hardness first increased, then decreased, and finally stabilized with the increasing number of deposition layers. The maximum hardness of as-built wall is ~685.4 HV$_{0.2}$. It is worth noting that the value was obtained after the indentation recovery which is due to the superelasticity effect of as-built wall. Due to the superelasticity phenomenon, the indentation size is reduced, which leads to a lower hardness value compared with the theoretical value. Thereby, the proper hardness of maximum hardness near the substrate is more than 685.4 HV$_{0.2}$. The increase in hardness near the substrate was due to its dilution effect. Therefore, numerous NiTi$_2$ phase generated. According to Fig. 3(a), NiTi$_2$ phase accounts for 38 %, which is the main reason of higher hardness distribution near the substrate. With the increasing of the distance away from substrate, the Ti content and dilution action decreased. The substrate turned into the B2 (NiTi) phase, and the hardness tended to be stable at 553 HV$_{0.2}$. The microhardness of the Ti–Ni–Al–V alloy fabricated by D-WAAM was stabilized at 553 HV$_{0.2}$. The microhardness is obviously greater than that of the NiTi alloy (278 HV$_{0.2}$), and the hardness increased by 98 %, mainly because of the solid solution of Al and V atoms. The Al and V atoms are present in the matrix and precipitate as a solid solution, thus realizing solid-solution strengthening.

A hardness contour of 7 mm × 7 mm from the top region was measured at 1-mm intervals. As shown in Fig. 4(b), the global hardness range is between 445 and 545.5 HV$_{0.2}$. The region with the highest hardness was largely relied on the quantity and distribution of the NiTi$_2$ or Ni$_4$Ti$_3$ phases. When the hard-precipitated phase of NiTi$_2$ was present, the hardness of the component was significantly improved. The precipitation strengthening generated by the Ni$_4$Ti$_3$-precipitated phase also significantly increased the microhardness of the component. The other parts with lower hardness are the NiTi matrix with less Al in the solid solution, and the regions with less precipitated phase content are shown in blue.

The compression curve of the Ti–Ni–Al–V specimen with a compressive strength of 2100 ± 15 MPa and compressive strain of 8.7 % ± 0.6 % MPa is shown in Fig. 5(a). In Fig. 5(c) and (d), the compression fracture is represented by a brittle river pattern. Furthermore, several cracks and shedding are observed, which are characteristics of brittle fractures. The main component phase in the fracture was NiTi, according to points 7 and 8. In Fig. 5(b), for cyclic compression, the recoverable and unrecoverable strains are 4.79 % and 1.21 %, respectively. With the continuous load cycle, the stress hysteresis decreases gradually, and the recoverable strain approached to a constant value. Because the stress promotes the formation of martensite, therefore, the D-WAAM technology produces uneven microstructure and the second phase, which leads to the phenomenon of stress concentration in some positions during the process of loading and unloading. The stress concentration is the main reason for the plastic strain of the matrix.

4. Conclusions

In this study, pure Ni and Ti–6Al–4V wires were used originally as raw materials to prepare a novel Ti–Ni alloy using D-WAAM. The conclusions are drawn.

(1) The as-built wall was composed of NiTi$_2$, B$_2$, and Ni$_4$Ti$_3$ phases from the bottom to the top. With an increase in deposition layers, the Ti$_2$Ni content decreased. Al and V are mainly soluble in the B2 phase.
(2) The hardness at the bottom was ~685.4HV$_{0.2}$, while that of the middle and stable regions was 553 HV$^{0.2}$. The overall hardness of the top region was distributed between 445 and 545.5HV$_{0.2}$.
(3) The maximum compressive strength was 2100 MPa. The fracture was brittle. After cyclic compression, the recoverable and unrecoverable strains were 4.79 % and 1.21 %, respectively, indicating excellent recovery characteristics.

Data availability statement

The authors do not have permission to share data.

Table 1
SEM and EDS evaluations (at.%).

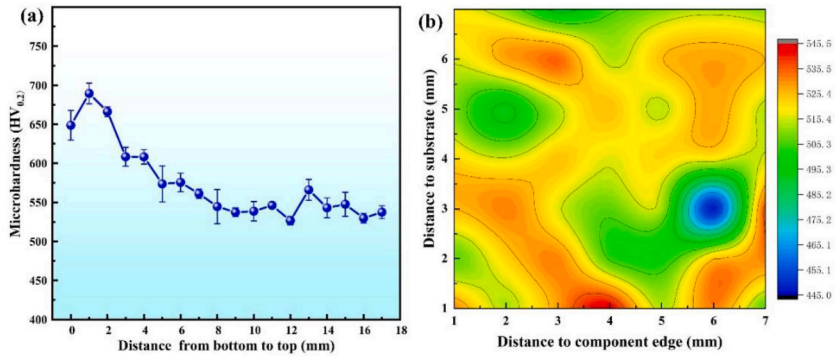| Position	Ti	Ni	V	Al	Possible phase
1 (Fig. 3)	47.47	47.10	–	5.43	NiTi
2 (Fig. 3)	57.84	31.61	2.00	8.55	NiTi$_2$
3 (Fig. 3)	47.51	46.68	–	5.81	NiTi
4 (Fig. 3)	56.97	31.23	2.53	9.27	NiTi$_2$
5 (Fig. 3)	46.19	47.82	–	5.99	NiTi
6 (Fig. 3)	56.98	30.04	4.18	8.80	NiTi$_2$
7 (Fig. 5)	45.88	48.35	–	5.77	NiTi
8 (Fig. 5)	45.91	48.18	–	5.91	NiTi

Fig. 4. (a) Hardness distribution and (b) hardness contour in the top region.
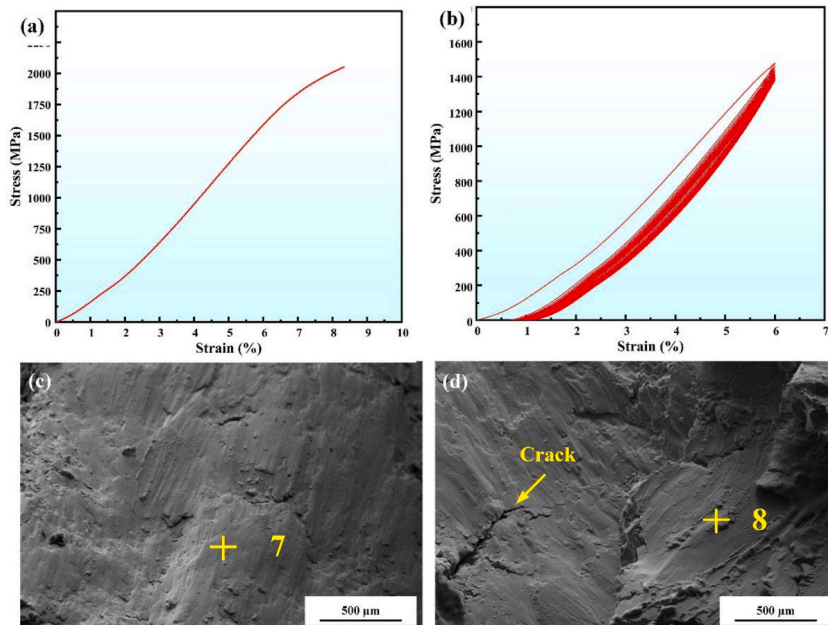

Fig. 5. Compression and cyclic compression results: (a) compression and (b) cyclic compression curves. (c, d) SEM image of the compression fracture.

CRediT authorship contribution statement

Xiaoxin Zhao: Writing - review & editing, Supervision, Methodology, Funding acquisition, Conceptualization. **Xinya Chen:** Writing - original draft. **Tao Ma:** Supervision, Resources. **Peng Zhang:** Supervision, Resources. **Jianguo Li:** Investigation. **Xin Zhang:** Investigation.

Declaration of competing interest

The authors declare that they have no known competing financial interests or personal relationships that could have appeared to influence the work reported in this paper.

Acknowledgements

References

[1] L. Wang, T. Wu, D. Wang, et al., A novel heterogeneous multi-wire indirect arc directed energy deposition for in-situ synthesis Al-Zn-Mg-Cu alloy: process, microstructure and mechanical properties, Addit. Manuf. (2023) 103639.

[2] Y. Tian, X. Chen, Y. Cai, et al., Microstructure and properties of a Ni–Ti–Cr–Mo–Nb alloy fabricated in situ by dual-wire arc additive manufacturing, Mater. Sci. Eng. 853 (2022) 143740.

[3] C. Shen, M. Reid, K.D. Liss, et al., In-situ neutron diffraction study on the high temperature thermal phase evolution of wire-arc additively manufactured Ni53Ti47 binary alloy, J. Alloys Compd. 843 (2020) 156020.

[4] J. Han, G. Zhang, X. Chen, et al., Fabrication and study of innovative Ni-added Ti–6Al–4V through directed energy deposition, Mater. Sci. Eng. 856 (2022) 143946.

[5] J. Wang, Z. Pan, G. Yang, et al., Location dependence of microstructure, phase transformation temperature and mechanical properties on Ni-rich NiTi alloy fabricated by wire arc additive manufacturing, Mater. Sci. Eng. 749 (2019) 218–222.

[6] A. Shuitcev, D.V. Gunderov, B. Sun, et al., Nanostructured Ti29.7Ni50.3Hf20 high temperature shape memory alloy processed by high-pressure torsion, J. Mater. Sci. Technol. 52 (2020) 218–225.

[7] G. Liu, S. Zhou, P. Lin, et al., Analysis of microstructure, mechanical properties, and wear performance of NiTi alloy fabricated by cold metal transfer based wire arc additive manufacturing, J. Mater. Res. Technol. 20 (2022) 246–259.

[8] H.Z. Lu, H.W. Ma, Y. Yang, et al., Tailoring phase transformation behavior, microstructure, and superelasticity of NiTi shape memory alloys by specific change of laser power in selective laser melting, Mater. Sci. Eng. 864 (2023) 144576.

[9] M. Tsaturyants, V. Sheremetyev, S. Dubinskiy, et al., Structure and properties of Ti–50.2 Ni alloy processed by laser powder bed fusion and subjected to a combination of thermal cycling and heat treatments, Shape Memory and Superelasticity 8 (1) (2022) 16–32.

[10] M. Zhang, X. Fang, Y. Wang, et al., High superelasticity NiTi fabricated by cold metal transfer based wire arc additive manufacturing, Mater. Sci. Eng. 840 (2022) 143001.

[11] J.Z. Teng, P.F. Jiang, X.H. Cui, et al., Revealing microstructural evolutions, mechanical properties and wear performance of wire arc additive manufacturing homogeneous and heterogeneous NiTi alloy, J. Mater. Res. Technol. 27 (2023) 1593–1610.

[12] J. Han, X. Chen, G. Zhang, et al., Microstructure and Mechanical Properties of NiTi AlloyPrepared by Double-Wire Plus Arc Additive Manufacturing Plus in Situ Heat Treatment[J]. 3D Printing and Additive Manufacturing, 00, 2023, https://doi.org/10.1089/3dp.2023.0003. DOI:.

[13] X. Xi, D. Lin, X. Song, et al., Strength-plasticity transition mechanism after the solution treatment of GH3230 superalloy fabricated via laser powder bed fusion, Mater. Sci. Eng. 876 (2023) 145124.

[14] D. Lin, X. Xi, X. Li, et al., High-temperature mechanical properties of FeCoCrNi high-entropy alloys fabricated via selective laser melting, Mater. Sci. Eng. 832 (2022) 142354.

[15] P.F. Zou, C.H. Zheng, L. Hu, et al., Rapid Growth of TiNi intermetallic compound within undercooled Ti50Ni50 alloy under electrostatic levitation condition, J. Mater. Sci. Technol. 77 (2021) 82–89.